Noname manuscript No.
(will be inserted by the editor)

Traditional Machine Learning for Limited Angle Tomography

Yixing Huang[1] · **Yanye Lu**[1] ·
Oliver Taubmann[1,2,3] ·
Guenter Lauritsch[3] · **Andreas Maier**[1,2]

Received: date / Accepted: date

Abstract

Purpose The application of traditional machine learning techniques, in the form of regression models based on conventional, "hand-crafted" features, to artifact reduction in limited angle tomography is investigated.

Methods Mean-variation-median (MVM), Laplacian, Hessian, and shift-variant data loss (SVDL) features are extracted from the images reconstructed from limited angle data. The regression models linear regression (LR), multi-layer perceptron (MLP), and reduced-error pruning tree (REPTree) are applied to predict artifact images.

Results REPTree learns artifacts best and reaches the smallest root-mean-square error (RMSE) of 29 HU for the Shepp-Logan phantom in a parallel-beam study. Further experiments demonstrate that the MVM and Hessian features complement each other, whereas the Laplacian feature is redundant in the presence of MVM. In fan-beam, the SVDL features are also beneficial. A preliminary experiment on clinical data in a fan-beam study demonstrates that REPTree can reduce some artifacts for clinical data. However, it is not sufficient as a lot of incorrect pixel intensities still remain in the estimated reconstruction images.

Conclusion REPTree has the best performance on learning artifacts in limited angle tomography compared with LR and MLP. The features of MVM, Hessian, and SVDL are beneficial for artifact prediction in limited angle tomography. Preliminary experiments on clinical data suggest that the investigation on more features is necessary for clinical applications of REPTree.

Keywords Machine learning · Limited angle tomography · Decision tree

✉ E-mail: yixing.yh.huang@fau.de, yanye.lu@fau.de
OrcidID:0000-0003-2627-3077
[1] Pattern Recognition Lab, Friedrich-Alexander-Universität Erlangen-Nürnberg, Martensstr. 3, 91058 Erlangen, Germany
[2] Erlangen Graduate School in Advanced Optical Technologies (SAOT), Friedrich-Alexander-Universität Erlangen-Nürnberg, Paul-Gordan-Str. 6, 91052 Erlangen, Germany
[3] Siemens Healthcare GmbH, Siemensstr. 1, 91301 Forchheim, Germany

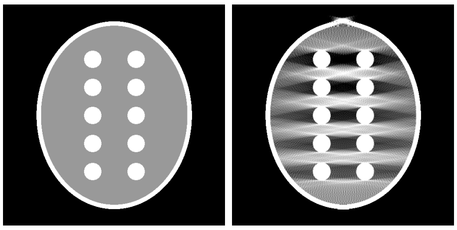

(a) Custom phantom (b) FBP reconstruction

Fig. 1 Demonstration of artifacts in limited angle tomography: a custom phantom (a) and its filtered back-projection (FBP) reconstruction (b) from 160° limited angle sinogram acquired in a limited angle scan (Fig. 2) in fan-beam geometry, window: [-300, 200] HU.

1 Introduction

C-arm angiographic devices are capable of acquiring 3-D images for planning, guiding, and monitoring of interventional operations. The 3-D images provide more detailed anatomical structures and better spatial information than conventional 2-D fluoroscopy images, which significantly facilitates the interventional operations. For image reconstruction in computed tomography (CT), a minimal angular range is required to acquire complete projection data, which is called a short scan. However, due to system restrictions, such a short scan is not achievable for some C-arm devices. In this case, some data are missing.

Image reconstruction from data acquired in an insufficient angular range is called limited angle tomography. Because of missing data, artifacts will occur in the reconstructed images. They cause boundary distortion, intensity leakage, and edge blurring as demonstrated in Fig. 1. Especially, a lot of streak artifacts occur along the missing angular ranges. Using microlocal analysis, edges that are tangent to available X-rays are well reconstructed while those whose singularities are not perpendicular to any X-ray lines cannot be reconstructed stably [1, 2].

So far, many interpolation/extrapolation methods are proposed to restore missing data in limited angle tomography [3–10]. Some are based on the iterative Papoulis-Gerchberg algorithm [3–7], which is popular to extrapolate band-limited signals. Some are based on consistency conditions like the well-known Helgason-Ludwig consistency conditions [8–10]. The reconstruction problem in limited angle tomography is severely ill-posed [11, 12], such that only low frequency parts of the missing frequency components of an imaged object are restored credibly while high frequency ones are not [10].

With the development of compressed sensing technologies, iterative reconstruction with total variation (TV) regularization becomes popular for limited angle tomography [13–18]. TV methods employ the prior knowledge that most medical images are sparse in the gradient domain. Hence, image quality can be improved. In addition, streak artifacts have certain orientations dependent on scan trajectories. Making use of such information, anisotropic TV algorithms are more effective to reduce artifacts than isotropic ones [16–18]. However, iterative algorithms are computationally expensive, which restrains their applications to interventional scenarios.

Recently, deep learning has outperformed the state of the art in various fields including CT [19, 20]. For limited angle tomography, Würfl et al. [21] propose a neural network to learn the compensation weights for limited angle data based on [22]. Hammernik et al. further add a variational network to eliminate coherent streak artifacts [23]. Gu and Ye adapt the U-Net architecture [24] to learn artifacts from streaky images in the multi-scale wavelet domain [25]. These methods can reduce artifacts in limited angle tomography well. Especially, the U-Net architecture, which is a fully convolutional neural network (CNN), has achieved impressive results for small scan angular ranges like 120° [25]. For deep learning, hand-crafted feature extraction is avoided since CNNs extract intrinsic features from high dimensional data by learning a number of small convolutional kernels [26].

Although deep learning has achieved impressive results in limited angle tomography, traditional machine learning techniques, i. e., a pixel-by-pixel prediction based on hand-crafted features, in limited angle tomography remains blank in literature. Therefore, in this paper we investigate three regression models in such a setup for limited angle tomography, namely, linear regression (LR), multi-layer perceptron (MLP), and reduced-error pruning tree (REPTree). In addition, feature extraction is crucial for traditional machine learning. Therefore, in this paper the influence of several selected features is investigated.

2 Materials and Methods

2.1 Input and Output

A general machine learning pipeline includes four main parts: input observations, feature extraction, a classification/regression model, and output labels. In this work, we choose the images reconstructed from the limited angle data (denoted by f_{limited}) as the input observations, and feature attributes will be extracted from them.

For the output of training, either artifact-free reference images (denoted by $f_{\mathsf{reference}}$) or residual artifact images (denoted by f_{artifact}, $f_{\mathsf{artifact}} = f_{\mathsf{limited}} - f_{\mathsf{reference}}$) can be chosen. Then the output of testing is an estimated artifact-free image or an estimated artifact image, correspondingly. In limited angle tomography, streak artifacts are the main artifacts and they share some similar features even though the artifact-free images are drastically different from each other. Therefore, Gu and Ye suggest that learning the artifact images is easier than learning the artifact-free images directly [25]. Hence, in this work we choose the artifact images as the output. Since we seek a pixel-by-pixel prediction based on hand-crafted features, each pixel value in the artifact images is an individual output label of a regression model.

2.2 Feature Extraction

Streak artifacts in limited angle tomography appear evidently near object boundaries. They are closely associated with object edges and have certain directions that are mainly determined by the acquisition geometry. Edges along directions of missing X-rays cause streaks in the same directions. Therefore, the following features are used for streak artifact prediction.

Mean-variation-median (MVM) At each position (x, y), the intensity of $f_{\mathsf{artifact}}(x, y)$ is highly related to the intensity of $f_{\mathsf{limited}}(x, y)$. Therefore, the intensity of $f_{\mathsf{limited}}(x, y)$ is one feature. As it is difficult to predict streak artifacts from a single pixel, the information of its neighborhood, typically an image patch, is necessary. Storing all the raw neighboring pixel values is memory expensive. Instead, the neighborhood can be characterized by the mean, variance, and median statistic.

Laplacian The Laplacian, or the Laplace operator, is one of the most popular edge detectors. It is a second order differential operator, which is defined as,

$$\Delta f(x, y) = \nabla^2 f(x, y) = \frac{\partial^2 f(x, y)}{\partial x^2} + \frac{\partial^2 f(x, y)}{\partial y^2}. \tag{1}$$

Hessian The Hessian matrix is a structure tensor constructed by second-order partial derivatives. It describes the local curvature of an image. The image $f(x, y)$ is first smoothed by a Gaussian kernel $G_s(x, y)$ with a standard deviation s, i. e., $f_s(x, y) = f(x, y) * G_s(x, y)$. The Hessian matrix at position (x, y) is computed as,

$$H_s(x, y) = \begin{bmatrix} \frac{\partial^2 f_s(x,y)}{\partial x^2} & \frac{\partial^2 f_s(x,y)}{\partial x \partial y} \\ \frac{\partial^2 f_s(x,y)}{\partial y \partial x} & \frac{\partial^2 f_s(x,y)}{\partial y^2} \end{bmatrix}. \tag{2}$$

Using the singular value decomposition, the two eigenvalues λ_1 and λ_2 ($\lambda_1 \geq \lambda_2$), and the two eigenvectors $\boldsymbol{v}_1$ and $\boldsymbol{v}_2$ can be computed. We pick the X direction as a reference direction and the orientation of the local curvature w. r. t. it is,

$$d = \arccos([1, 0]^\top \cdot \boldsymbol{v}_1 / ||\boldsymbol{v}_1||). \tag{3}$$

In this paper, λ_1, λ_2, and d are the selected Hessian features.

Shift-variant data loss (SVDL) In our experimental setting, the detector is always large enough to cover the projection of the whole imaged object. With such a constraint, different points at different locations have the same angular range of X-rays passing through them in parallel-beam limited angle tomography. However, in fan-beam limited angle tomography, different points at different locations have different angular ranges of X-rays missing, which we call shift-variant data loss. In a circular fan-beam trajectory, we denote the start and end rotation angles of an X-ray source by $\beta_{\min}$ and $\beta_{\max}$, respectively, and the source-to-isocenter distance by D. As displayed in Fig. 2, when the X-ray source rotates from the start position S_0 to the end position s_1, X-rays between the directions of η_1 and η_2 can pass through a point $\boldsymbol{x}(x, y)$. The two angles can be calculated as,

$$\eta_1 = \operatorname{atan}\left(\frac{y + D\sin\beta_{\min}}{D\cos\beta_{\min} - x}\right), \qquad \eta_2 = \operatorname{atan}\left(\frac{x - D\cos\beta_{\max}}{y + D\sin\beta_{\max}}\right) + \frac{\pi}{2}, \tag{4}$$

which are dependent on the position of the point $\boldsymbol{x}$ and can indicate the orientations of streak artifacts. We further denote the covered angular range by $\Delta\eta$, where $\Delta\eta = \eta_2 - \eta_1$ and typically $\Delta\eta < \pi$ in limited angle tomography. When $\Delta\eta$ is small, it is very likely to have artifacts at point $\boldsymbol{x}$. Since picking two of the three parameters η_1, η_2, and $\Delta\eta$ is sufficient to describe the covered angular region, we choose η_1 and $\Delta\eta$ as the SVDL features in this paper.

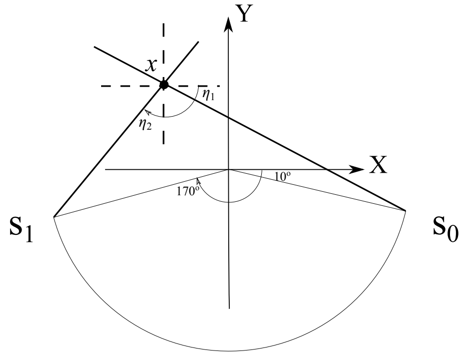

Fig. 2 The scan trajectory in fan-beam limited angle tomography and a sketch of the shift-variant data loss model. The X-ray source rotates from $s_0(\beta_{\min} = 10°)$ to $s_1(\beta_{\max} = 170°)$. The rays with angles η_1 and η_2 are the rays passing through the point $\boldsymbol{x}$ with the minimum and the maximum angles, respectively.

2.3 Regression Models

In this paper, we investigate the following three regression models.

Linear Regression Linear regression is the most popular method in many statistical applications. It expresses the output label as a linear combination of the extracted feature attributes and the trained weights.

Multi-layer Perceptron MLP [27, 28] can learn more complex, nonlinear functions than linear regression. MLP generally contains an input layer, several hidden layers, and an output layer. At hidden layers, nonlinear activation functions like the sigmoid activation function are typically used. The backpropagation method with stochastic gradient descent method is used for training.

Reduced-Error Pruning Tree A decision tree utilizes a tree-like structure to predict an output from the feature attributes. A tree is learnt recursively by splitting the training data set into subsets based on attribute value tests. The recursion process stops when the subset at a node has all the same value, or the tree reaches the maximum depth. Gini impurity or information gain is typically used to obtain an optimal attribute order for splitting [29]. A pruning process is employed to prevent overfitting. In this paper, we use the reduced-error pruning tree (REPTree) [30] which is a simple and fast pruning method. The pruning starts at the leaves and each node is replaced with its most popular class value. The change is kept if the resulting tree performs no worse than the original on the validation set. The REPTree algorithm uses the information gain for splitting.

2.4 Workflow

A flowchart summarizing our implementation of machine learning algorithms for limited angle tomography is displayed in Fig. 3. For an input limited angle reconstruction image f_{limited}, at pixel/position (x, y), an image patch is generated and features of MVM, Laplacian, Hessian, or SVDL are extracted from this patch. The extracted features form a feature vector $\boldsymbol{x}$. With a trained regression model, the intensity of f_{artifact} at pixel (x, y) is estimated, denoted by $I_{x,y}$ in the flowchart. When

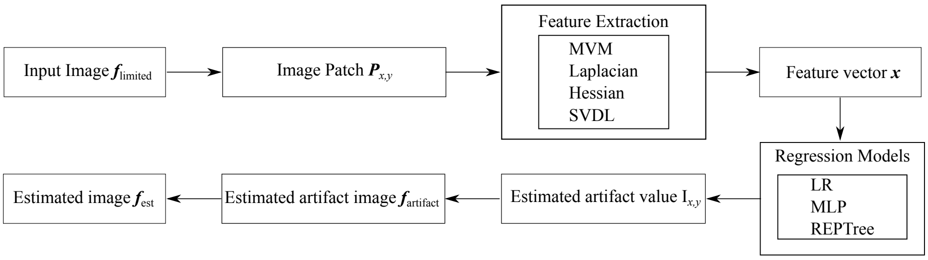

Fig. 3 A flowchart summarizes our implementation of machine learning algorithms for limited angle tomography.

the values $I_{x,y}$ of all the pixels are estimated, the artifact image f_{artifact} is obtained. Then the artifact reduced image is estimated, denoted by $f_{\text{est}} = f_{\text{limited}} - f_{\text{artifact}}$.

2.5 Experimental Set-up

To initially check the validity of different features and regression models, a 3-D standard high-contrast pixelized Shepp-Logan phantom is generated. Its pixel value is at the range of [0, 1], which is converted to [-1000, 1000] HU in the Hounsfield unit. Its image size is $512 \times 512 \times 200$. The pixel size is 0.4 mm in X and Y directions and 1.024 mm in Z direction. We pick 150 slices from the 3-D volume and one half of them are used for training, the other half for validation.

We first investigate the effects of different regression models and different features in parallel-beam using the selected Shepp-Logan images. In parallel-beam, the angles η_1 and $\Delta\eta$ for different position points are all the same. Therefore, the SVDL features are omitted here. We reproject the images using a ray-driven method with a sampling rate of 7.5/mm. No noise is simulated. The scanned angular range is 160°. The angular step is 0.5°. The number of the equal-space detector pixels N_D is 1537 and the detector element size is 0.2 mm.

To validate the application of REPTree in fan-beam and further investigate the effect of the SVDL features, a fan-beam study is conducted using the same selected Shepp-Logan images. The images are reprojected in a fan-beam geometry. The angular increment is 0.5°. The detector has 1536 pixels and the pixel size is 0.4 mm. The source-to-detector distance is 1740 mm and the source-to-isocenter distance is 870 mm. The fan angle is 20°. The scan angular range is 160°.

As preliminary experiments for clinical data, 18 patients' CT data from the Low Dose CT Grand Challenge [31] are used, 8 patients for training, another 8 patients for validation, and 2 patients for testing. For each patient, we pick 10 slices. Each slice is 20 mm away from its neighboring slices and has a size of 512×512 with an isotropic pixel size of 0.625 mm. The selected images are reprojected in the same fan-beam geometry as the fan-beam Shepp-Logan experiment. The REPTree model is retrained using the MVM, Hessian, and SVDL features.

The images f_{limited} are reconstructed using filtered backprojection (FBP) with the Ram-Lak filter from the limited angle projections for both the Shepp-Logan data and the clinical data.

The machine learning algorithms are based on the Waikato Environment for Knowledge Analysis (Weka) [32]. MLP uses four hidden layers. The learning rate,

Fig. 4 The reference slice of the Shepp-Logan phantom shown in window [-700, -500] HU.

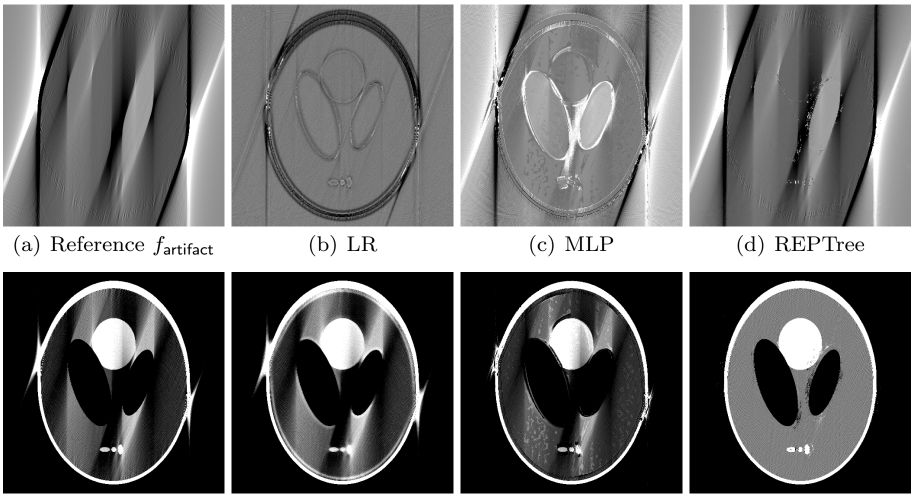

(a) Reference f_{artifact} (b) LR (c) MLP (d) REPTree

(e) f_{limited}, 140.2 HU (f) LR, 139.0 HU (g) MLP, 133.4 HU (h) REPTree, 29.3 HU

Fig. 5 Learnt artifact images using different machine learning algorithms and their corresponding reconstructed images in parallel-beam with a 160° trajectory (from −80° to 80° in Fig. 2). The MVM, Laplacian, and Hessian features are used. The RMSE of the estimated images is displayed in the subcaptions (e)-(h). Window width for the top row: 400 HU; window for the bottom row: [-700, -500] HU.

the momentum, and the epochs are set to 0.3, 0.2 and 100, respectively. REPTree sets 1 as the minimum number of instances per leaf node and the maximum depth of the tree is set to be unlimited. The MVM features are extracted from quadratic image patches of side length 2, 4, 8 and 16. For the Hessian features, the standard deviation s is set to 9 pixels. The whole implementation is based on CONRAD [33].

3 Results

3.1 Parallel-beam Numerical Data

The center slice (Fig. 4) of the validation dataset of the Shepp-Logan phantom is picked as an example to show the effects of different regression models. Fig. 5 displays the results of different regression models using all the features of MVM,

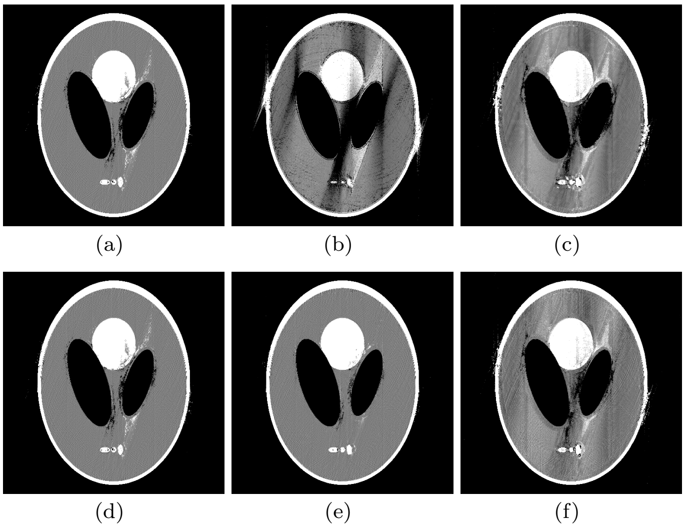

Fig. 6 The results of REPTree using different feature combinations in parallel-beam with a 160° trajectory: (a) MVM, (RMSE =) 38.4 HU; (b) Laplacian, 119.2 HU; (c) Hessian, 76.48 HU; (d) MVM and Laplacian, 38.5 HU; (e) MVM and Hessian, 28.9 HU; (f) Laplacian and Hessian, 65.0 HU. Window: [-700, -500] HU.

Laplacian, and Hessian in parallel-beam. Compared with the reference streak artifact image (Fig. 5(a)), LR misclassifies the edges as streak artifacts and recognizes few streaks (Fig. 5(b)). MLP can recognize streak artifacts better than LR, but it still misclassifies the edges as artifacts (Fig. 5(c)). Instead, REPTree classifies most streak artifacts correctly with only minor misclassifications (Fig. 5(d)). By subtracting the learnt streak artifacts, the "destreaked" images are estimated in Figs. 5(f)-(h). While streak artifacts remain in the results of LR and MLP, most of them are reduced by REPTree. The root-mean-square error (RMSE) of the destreaked images w. r. t. the reference image (Fig. 4) is further computed. REPTree reaches the smallest RMSE value of 29.3 HU.

To investigate the effects of different features in streak artifact classification, the results of REPTree using different combinations of features for the Shepp-Logan data in parallel-beam are shown in Fig. 6. As mentioned before, the SVDL features are omitted here since all the pixels at different positions have the same SVDL features in parallel-beam. Figs. 6(a)-(c) indicate that using MVM only is able to predict most artifacts while using Laplacian or Hessian only is not sufficient. Fig. 6(f) shows that the combination of Laplacian and Hessian is even worse than MVM only, which indicates that MVM is important to predict streak artifacts. Comparing Fig. 6(d) with Fig. 6(a), the Laplacian feature is redundant in the presence of MVM since Fig. 6(d) and Fig. 6(a) have almost the same image quality. Fig. 6(e) and Fig. 5(h) also demonstrate that skipping the Laplacian feature does not change image quality. Fig. 6(e) indicates that the Hessian features are beneficial, compared with Fig. 6(a).

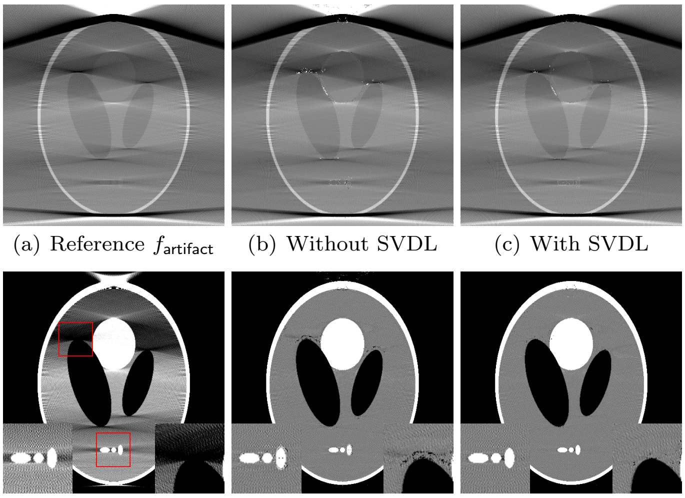

(a) Reference f_{artifact} (b) Without SVDL (c) With SVDL

(d) f_{limited} (e) Without SVDL (f) With SVDL

Fig. 7 The effect of the SVDL features in fan-beam with a 160° trajectory. The top row images are the reference artifact image and the learnt artifact images by REPTree without or with the SVDL features along with the MVM and Hessian features displayed in a window width of 400 HU. The bottom row images are the corresponding reconstructed images displayed in window [-700, -500] HU. Two ROI (marked as the red squares in (d)) images are shown at the left bottom corner and the right bottom corner, respectively. The RMSE for (d)-(f) are 132 HU, 37 HU, and 34 HU, respectively.

3.2 Fan-beam Numerical Data

The fan-beam results of the center slice of the Shepp-Logan data are displayed in Fig. 7. Fig. 7(b) is the learnt artifact image by REPTree using the MVM and Hessian features. It demonstrates that REPTree can also learn most of the artifacts for the Shepp-Logan data in fan-beam. The corresponding reconstructed image is shown in Fig. 7(e), where most artifacts are reduced. However, some isolated pixels have strongly incorrect intensities which can be seen as black or white dots. They can be better seen at the region-of-interest (ROI) images displayed at the left and right bottom corners in Fig 7(e). The artifact image learnt by REPTree using the MVM, Hessian, and SVDL features is shown in Fig. 7(c) and the corresponding reconstruction image is shown in Fig. 7(f). Compared with Fig. 7(e), most of the incorrect pixel intensities are corrected in Fig. 7(f), which can be better seen at the ROI images in Fig 7(f). This demonstrates that the SVDL features are also beneficial for artifact reduction in limited angle tomography. We might note that the RMSE is not much affected since only isolated pixels are corrected.

The evaluation of the whole validation dataset is shown in Fig. 8 where the RMSE and the structural similarity (SSIM) indices [34] are computed. For the RMSE, its value gradually decreases from around 37 HU to 21 HU with some oscillations when the slice is from the center to the top or the bottom. Consistently, the SSIM index increases from around 0.996 to 0.998.

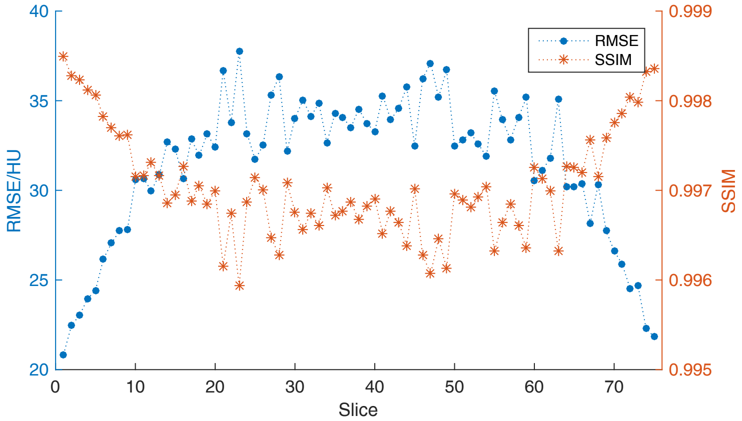

Fig. 8 The RMSE and SSIM indices of the validation slices of the Shepp-Logan data in fan-beam with a 160° trajectory.

3.3 Fan-beam Clinical Data

The preliminary experiments on the clinical data are displayed in Fig. 9. Comparing Fig. 9(c) with Fig. 9(b), most artifacts in Fig. 9(c) are reduced, which demonstrates that REPTree is also able to reduce some artifacts for clinical data. However, many isolated pixels have incorrect intensities in Fig. 9(f) (black dots). From Fig. 7 we already know that MVM and Hessian are insufficient in the fan-beam geometry. The SVDL features are able to correct most black dots for simple phantom data. However, they are not sufficient for clinical data. Therefore, more features have to be applied for clinical applications. The images in Fig. 9 are re-displayed in Fig. 10 using a small window where most soft tissues can be seen. In Fig. 10(c) and Fig. 10(f), most intensity biases are corrected comparing to Fig. 10(b) and Fig. 10(e), respectively. However, still many anatomical structures are obscured by the new artifacts introduced by REPTree. Figs. 9 and 10 reveal the limitation of REPTree in the application of clinical data.

The evaluation of the selected 20 testing slices from the 2 testing patients, Patient 1 and Patient 2, is shown in Fig. 11. The RMSE values of the estimated slices of Patient 1 are all around 63 HU while their SSIM indices are around 0.992. The RMSE values of the estimated slices of Patient 2 vary from 70 HU to 85 HU while their SSIM indices vary from 0.980 to 0.990.

4 Discussion

The mapping from the selected feature attributes to the streak artifacts is a complex nonlinear function. Therefore, LR fails to model that. Although a large MLP with enough hidden units can model any nonlinear functions, in our case, MLP fails to find the desired function during training. REPTree represents the mapping function well with enough nodes and it reduces the overfitting problem with pruning. Therefore, REPTree performs best in the experiments (Fig. 5).

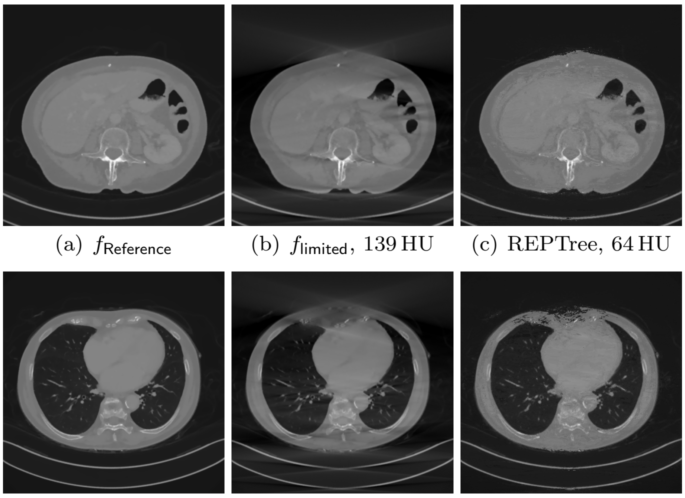

(a) $f_{\mathsf{Reference}}$ (b) f_{limited}, 139 HU (c) REPTree, 64 HU

(d) $f_{\mathsf{Reference}}$ (e) f_{limited}, 141 HU (f) REPTree, 85 HU

Fig. 9 The reference images, the limited angle reconstructions, and the machine learning results using REPTree with the MVM, Hessian, and SVDL features of two patients in fan-beam with a 160° trajectory. Window: [-1200, 1400] HU.

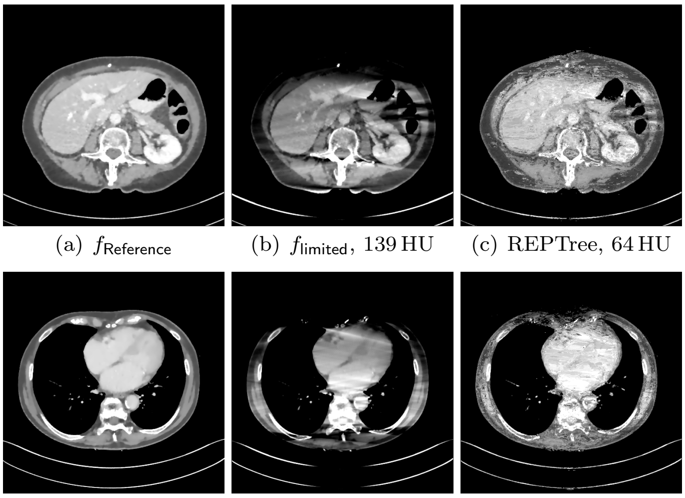

(a) $f_{\mathsf{Reference}}$ (b) f_{limited}, 139 HU (c) REPTree, 64 HU

(d) $f_{\mathsf{Reference}}$ (e) f_{limited}, 141 HU (f) REPTree, 85 HU

Fig. 10 The images in Fig. 9 are redisplayed in a small window [-200, 200] HU.

The Laplacian feature is redundant in the presence of MVM (Fig. 6). As a potential reason, one has to consider that the Laplacian is just a linear combination of the neighboring pixels described by MVM. The Hessian features are beneficial since they stress on the strength as well as the orientation of local curvatures, which are essential properties of limited angle streak artifacts. The SVDL features indicate the orientations of streak artifacts. They also tell the amount of missing information at different positions. Therefore, the SVDL features are also beneficial.

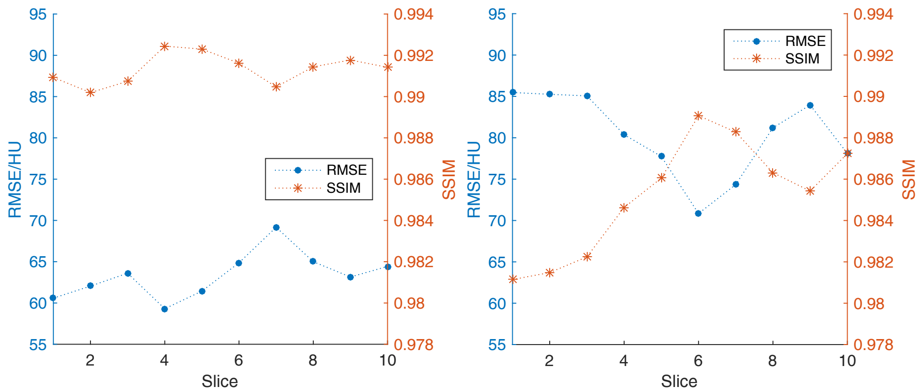

(a) Patient 1 (b) Patient 2

Fig. 11 The RMSE and SSIM indices of the testing slices of the clinical data in fan-beam with a 160° trajectory. Slice 10 of Patient 1 corresponds to Fig. 9(c) and Slice 1 of Patient 2 corresponds to Fig. 9(f).

In the Shepp-Logan experiments, the training data and the validation data share a lot of similarities, since both of them are selected from the 3-D Shepp-Logan phantom. Nevertheless, these experiments are sufficient to validate whether a regression model is able to represent the mapping function between the output pixel value and the selected features in the ideal case. However, the clinical data are much more complex than the Shepp-Logan data. Therefore, REPTree is not sufficient to reduce all artifacts, although it is able to reduce some of them (Fig. 9). Especially, in this paper, we use a pixel-by-pixel prediction based on hand-crafted features from its neighborhood. In this setting, the prediction result of each pixel is somewhat independent on its neighboring prediction results, even though we select the neighboring information via the MVM features in the input images. Therefore, the context of the image is lost and isolated dark areas occur (Fig. 9(f)).

5 Conclusion

In summary, we investigate the application of LR, MLP, and REPTree for artifact reduction in limited angle tomography. The experiments on the Shepp-Logan phantom demonstrate that REPTree has the best performance on learning artifacts compared with LR and MLP. They also indicate that MVM, Hessian, and SVDL features are beneficial for artifact prediction while the Laplacian is redundant in the presence of MVM. The preliminary experiment on clinical data shows the limitation of REPTree and the selected features. It indicates that further improvement of REPTree is necessary for clinical applications.

Compliance With Ethical Standards:

Conflict Of Interest Disclosure: Oliver Taubmann and Guenter Lauritsch are with Siemens Healthcare GmbH, Forchheim, Germany. Yixing Huang is supported by Siemens Healthcare GmbH, Forchheim, Germany.

Ethical Approval And Informed Consent: The clinical data in this paper are from the library of the Low Dose CT Grand Challenge [31]. The library was HIPAAcompliant and built with waiver of informed consent. All data shared in the challenge were fully anonymized.

This article does not contain any studies with animals performed by any of the authors.

Disclaimer: The concepts and information presented in this paper are based on research and are not commercially available.

References

1. E.T. Quinto, An introduction to X-ray tomography and Radon transforms, Proc Symp APPl Math **63**, 1 (2006)
2. E.T. Quinto, Local algorithms in exterior tomography, J Comput Appl Math **199**(1), 141 (2007)
3. F.A. Grünbaum, A study of Fourier space methods for limited angle image reconstruction, Numer Funct Anal Optim **2**(1), 31 (1980)
4. M. Defrise, C. De Mol, A regularized iterative algorithm for limited-angle inverse Radon transform, Opt Acta: Int J Opt **30**(4), 403 (1983)
5. G.R. Qu, Y.S. Lan, M. Jiang, An iterative algorithm for angle-limited three-dimensional image reconstruction, Acta Math Appl Sin **24**(1), 157 (2008)
6. G.R. Qu, M. Jiang, Landweber iterative methods for angle-limited image reconstruction, Acta Math Appl Sin **25**(2), 327 (2009)
7. Y. Huang, O. Taubmann, X. Huang, G. Lauritsch, A. Maier, Papoulis-Gerchberg algorithms for limited angle tomography using data consistency conditions, Procs CT Meeting pp. 189–192 (2018)
8. A.K. Louis, W. Törnig, Picture reconstruction from projections in restricted range, Math Methods Appl Sci **2**(2), 209 (1980)
9. A.S. Willsky, J.L. Prince, Constrained sinogram restoration for limited-angle tomography, Opt Eng **29**(5), 535 (1990)
10. Y. Huang, X. Huang, O. Taubmann, Y. Xia, V. Haase, J. Hornegger, G. Lauritsch, A. Maier, Restoration of missing data in limited angle tomography based on Helgason-Ludwig consistency conditions, Biomed Phys & Eng Express **3**(3), 035015 (2017)
11. M.E. Davison, The ill-conditioned nature of the limited angle tomography problem, SIAM J Appl Math **43**(2), 428 (1983)
12. A.K. Louis, Incomplete data problems in X-ray computerized tomography: I. singular value decomposition of the limited angle transform, Numerische Mathematik **48**(3), 251 (1986)
13. E.Y. Sidky, X. Pan, Image reconstruction in circular cone-beam computed tomography by constrained, total-variation minimization, Phys Med Biol **53**(17), 4777 (2008)
14. L. Ritschl, F. Bergner, C. Fleischmann, M. Kachelrieß, Improved total variation-based CT image reconstruction applied to clinical data, Phys Med Biol **56**(6), 1545 (2011)
15. J. Frikel, Sparse regularization in limited angle tomography, Appl Comput Harmon Anal **34**(1), 117 (2013)

16. Z. Chen, X. Jin, L. Li, G. Wang, A limited-angle CT reconstruction method based on anisotropic TV minimization, Phys Med Biol **58**(7), 2119 (2013)
17. T. Wang, K. Nakamoto, H. Zhang, H. Liu, Reweighted anisotropic total variation minimization for limited-angle CT reconstruction, IEEE Trans Nucl Sci **64**(10), 2742 (2017)
18. Y. Huang, O. Taubmann, X. Huang, V. Haase, G. Lauritsch, A. Maier, Scale-space anisotropic total variation for limited angle tomography, IEEE Trans Radiat Plasma Med Sci **2**(4), 307 (2018)
19. G. Wang, A perspective on deep imaging, IEEE Access **4**, 8914 (2016)
20. B. Zhu, J.Z. Liu, S.F. Cauley, B.R. Rosen, M.S. Rosen, Image reconstruction by domain-transform manifold learning, Nature **555**(7697), 487 (2018)
21. T. Würfl, M. Hoffmann, V. Christlein, K. Breininger, Y. Huang, M. Unberath, A.K. Maier, Deep learning computed tomography: Learning projection-domain weights from image domain in limited angle problems, IEEE Trans Med Imaging **37**, 0 (2018)
22. C. Riess, M. Berger, H. Wu, M. Manhart, R. Fahrig, A. Maier, TV or not TV? That is the Question, Procs Fully3D pp. 341–344 (2013)
23. K. Hammernik, T. Würfl, T. Pock, A. Maier, A deep learning architecture for limited-angle computed tomography reconstruction, Procs BVM pp. 92–97 (2017)
24. O. Ronneberger, P. Fischer, T. Brox, U-net: Convolutional networks for biomedical image segmentation, Procs MICCAI pp. 234–241 (2015)
25. J. Gu, J.C. Ye, Multi-scale wavelet domain residual learning for limited-angle CT reconstruction, Procs Fully3D pp. 443–447 (2017)
26. M.D. Zeiler, R. Fergus, Visualizing and understanding convolutional networks, Eur Conf Comput Vis pp. 818–833 (2014)
27. R. F, The perceptron - a probabilistic model for information-storage and organization in the brain, Psychol Rev **65**, 386 (1958)
28. T. Kohonen, An introduction to neural computing, Neural Netw **1**(1), 3 (1988)
29. W.Y. Loh, Classification and regression trees, Wiley Interdiscip Rev Data Min Knowl Discov **1**(1), 14 (2011)
30. J.R. Quinlan, Simplifying decision trees, Int J Man Mach Stud **27**(3), 221 (1987)
31. C.H. McCollough, A.C. Bartley, R.E. Carter, B. Chen, T.A. Drees, P. Edwards, D.R. Holmes, A.E. Huang, F. Khan, S. Leng, K.L. McMillan, G.J. Michalak, K.M. Nunez, L. Yu, J.G. Fletcher, Low-dose CT for the detection and classification of metastatic liver lesions: Results of the 2016 low dose CT grand challenge, Med Phys **44**(10) (2017)
32. E. Frank, M.A. Hall, I.H. Witten, *The WEKA workbench. Online appendix for "Data Mining: Practical Machine Learning Tools and Techniques"* (Morgan Kaufmann, 2016)
33. A. Maier, H. Hofmann, M. Berger, P. Fischer, C. Schwemmer, H. Wu, K. Müller, J. Hornegger, J. Choi, C. Riess, A. Keil, R. Fahrig, CONRAD - a software framework for cone-beam imaging in radiology, Med Phys **40**(11), 111914 (2013)
34. Z. Wang, A.C. Bovik, H.R. Sheikh, E.P. Simoncelli, Image quality assessment: from error visibility to structural similarity, IEEE Trans Image Process **13**(4), 600 (2004)